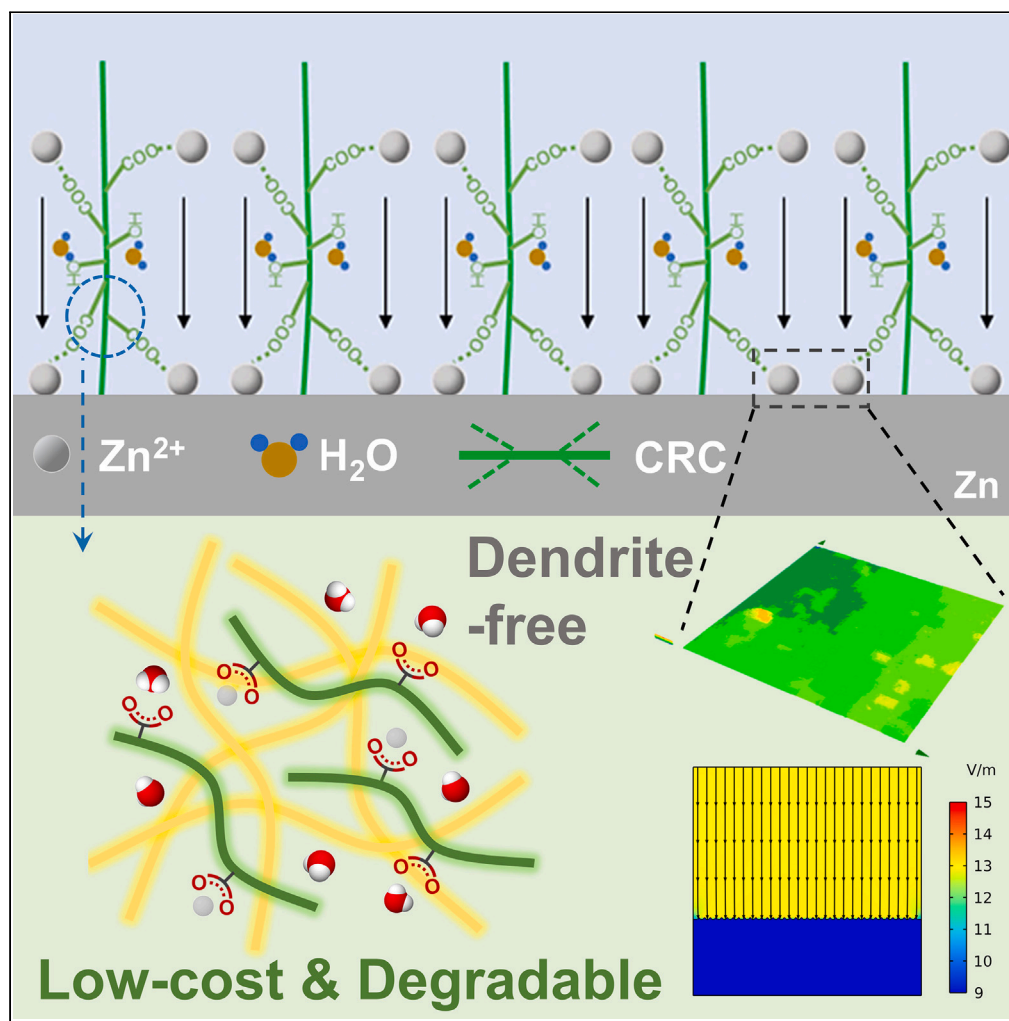**Article**

A bio-based functional separator enables dendrite-free anodes in aqueous zinc-ion batteries

Han Zhang, Jinbo
Li, Huaizheng Ren,
..., Dianlong Wang,
Huakun Liu, Shixue
Dou

wangbo19880804@163.com
(B.W.)
wangdianlonghit@163.com
(D.W.)

Highlights

Enhanced mechanical
properties effectively
inhibit dendrite growth

The binding to Zn^{2+}
exhibits uniform nucleation
and deposition

The reduced activity of
water hinders side
reactions

Markedly economical and
eco-friendly features reveal
potential in practical
applications

Article

A bio-based functional separator enables dendrite-free anodes in aqueous zinc-ion batteries

Han Zhang,[1] Jinbo Li,[1] Huaizheng Ren,[1] Jianxin Wang,[1] Yuxin Gong,[1] Bo Wang,[1,2,5,*] Dianlong Wang,[1,*] Huakun Liu,[3,4] and Shixue Dou[3,4]

SUMMARY

Aqueous zinc-ion batteries (AZIBs) have garnered considerable interest as potential solutions for large-scale energy storage systems, owing to their cost-effectiveness and high safety. Nonetheless, the development of AZIBs is hindered by significant challenges associated with dendrite growth and side reactions on Zn anodes. Here, a bio-based separator derived from cellulose was developed for the dendrite-free anode in AZIBs. In addition, the separator is notable for its ultra-low cost and biodegradability in contrast to the commonly used commercial glass fiber (GF) separators. The mechanical strength of the separator is enhanced by the cross-linking of hydrogen bonds, effectively inhibiting dendrite growth. The zinc-philic groups facilitate better binding to Zn^{2+}, resulting in uniform nucleation and deposition. The hydrophilic groups aid in trapping water molecules, thereby preventing side reactions of the electrolyte. The Zn|| Zn symmetric cell with this separator can sustain a long cycle life for over 800 h, indicating stable Zn^{2+} plating and stripping with suppressed dendrite growth. Concurrently, the assembled Zn||VO_2 full batteries exhibited a capacity retention rate of 61.87% after 1,000 cycles at 1 A g^{-1} with an initial capacity of 140 mAh g^{-1}. This work highlights a stable, economical, and eco-friendly approach to the design of bio-based separators in AZIBs for sustainable energy storage systems.

INTRODUCTION

Aqueous zinc-ion batteries (AZIBs) have attracted significant attention as a promising alternative to lithium-ion batteries (LIBs) for large-scale energy storage systems due to their high theoretical capacity, low redox potential, high safety, and eco-friendliness.[1] Despite the enormous potential of AZIBs for developing novel battery systems, several unresolved issues persist.[2] The application of AZIBs is mainly impeded by two concerns associated with the Zn anode: dendrite growth and water-related side reactions.[3] On one hand, the irregular deposition of Zn^{2+} exacerbates uneven electric field distribution and eventually leads to severe dendrite growth.[4] Zn dendrites in large quantities can easily puncture the separator and cause battery failure. On the other hand, the use of aqueous electrolytes leads to hydrogen evolution reaction (HER) and the formation of zinc hydroxide sulfate (ZHS), inducing the consumption of electrolytes and battery expansion.[5]

To address the aforementioned problems, many solutions have been proposed, including electrolyte additives,[6] collector modification,[7] separator modification,[8] and functional separator design.[9] As carriers for aqueous electrolytes, separators require toughness, flexibility, hydrophilicity, and uniform pore size distribution, which can regulate Zn^{2+} flux and electric field distribution on Zn anodes.[9] Apart from electrochemical performances, the cost and environmental compatibility must also be taken into account.[10] Currently, glass fiber (GF) separators are the most commonly used separator in AZIBs. Although GF separators offer high porosity and excellent liquid absorption, some flaws remain.[11] First, non-uniform large-scale pores in GF may result in irregular Zn^{2+} deposition and lead to severe dendrite growth.[12] Second, their thickness and looseness make it challenging to achieve high energy density in battery assembly.[13] After all, commercial GF separators are expensive and cannot naturally degrade after disposal. Hence, there is a practical trend to develop multifunctional alternative separators suitable for AZIBs.

Considering the cost and biodegradability of the potential alternative separator, cellulose, the most abundant biopolymer material in nature,[14] emerges as a suitable choice.[14–19] Cellulose-based materials have many advantages such as sustainability, renewability, biocompatibility, biodegradability, and non-toxicity.[14,19] By extracting 1D nanomaterials with a diameter of less than 100 nm from microcrystalline cellulose, cellulose nanofibers (CNFs) can be obtained.[16] Compared to 2D and 3D cellulose, CNFs exhibit a larger surface area and higher porosity and the nano lines contribute significant strength and directional stability.[20] Therefore, cellulose-based separators have shown more comprehensive performance among various materials of many separators.[21–25] Recently, a number of novel cellulose-based separators

[1]MIIT Key Laboratory of Critical Materials Technology for New Energy Conversion and Storage, State Key Laboratory of Urban Water Resource and Environment, School of Chemistry and Chemical Engineering, Harbin Institute of Technology, Harbin 150001, China
[2]Key Laboratory of Advanced Energy Materials Chemistry (Ministry of Education), College of Chemistry, Nankai University, Tianjin 300071, China
[3]Institute of Energy Material Science, University of Shanghai for Science and Technology, Shanghai 200093, China
[4]Institute for Superconducting & Electronic Materials, Australian Institute of Innovative Materials, University of Wollongong, Wollongong, NSW 2500, Australia
[5]Lead contact
*Correspondence: wangbo19880804@163.com (B.W.), wangdianlonghit@163.com (D.W.)
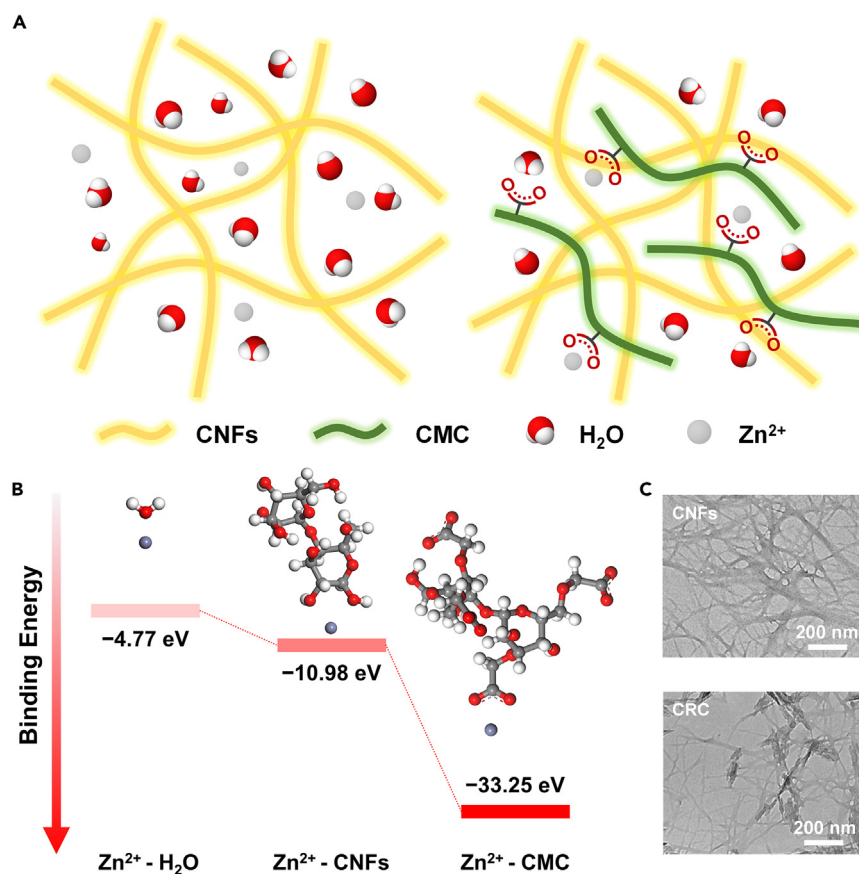https://doi.org/10.1016/j.isci.2024.110237

Figure 1. Synthesis and characterization of separators

(A) Schematic illustration of CNFs and CRC separators.

(B) Binding energy calculations based on DFT between Zn^{2+} and different components of CNFs and CRC.

(C) TEM images of CNFs and CRC.

have been developed for AZIBs.[26–30] For example, Wang et al. generated a cotton-derived cellulose separator, effectively inhibiting dendrites and side reactions on Zn anodes.[26] Herein, a low-cost and degradable separator derived from cellulose was proposed for dendrite-free anodes in AZIBs. In this work, the CNFs were used as the matrix and carboxymethyl cellulose (CMC) was used as the optimized component. The additive of CMC will further enhance the mechanical properties of cellulose-based separators[31] and demonstrate better Zn^{2+} binding and water trapping ability compared to CNFs.[30] Finally, CMC-reinforced CNFs (CRC) separators were obtained. The Zn‖Zn symmetric cell with this separator can sustain a long cycle life for over 800 h. The Zn‖VO$_2$ full cell exhibited a capacity retention rate of 61.87% after 1,000 cycles at 1 A g^{-1} with an initial capacity of 140 mAh g^{-1}. Moreover, considering adequate cycling performance, we introduce the crucial aspects of cost and degradability to the development of multifunctional alternative separators.

RESULTS AND DISCUSSION

Synthesis and characterization

CRC separators were prepared by a simple sol-gel method, and the detailed preparation and methods are shown in Figure S1. As shown in Figure 1A, CMC is rich in carboxyl and hydroxyl groups, which can interact with CNFs in the liquid phase. Chemical copolymerization necessitates cross-linking agents, which can restrict material biodegradability and raise processing costs.[30] In contrast to the approach taken in this study, the actual preparation process excluded cross-linking agents. In such conditions, cellulose chains aggregate by forming longitudinal networks through intermolecular hydrogen bonding.[15,16] Thus, the cost and degradability of the separator had improved. The composition of the two cellulose-based components of CRC can be observed by transmission electron microscope (TEM) images (Figure 1C). According to the structure of each component, hydroxyl and carboxyl groups contribute to hydrogen bonding in CMC, CNFs, and water, while carboxyl groups can interact with Zn^{2+} in the electrolyte. Figures 1B and S2 show the binding energy calculations based on density functional theory (DFT). Compared to water, groups of cellulose derivatives, especially the carboxyl groups, act as strong zinc-philic sites. This facilitates a more efficient and uniform migration of Zn^{2+} during the deposition, as evidenced by a binding energy of −33.25 eV between the Zn^{2+} and carboxyl
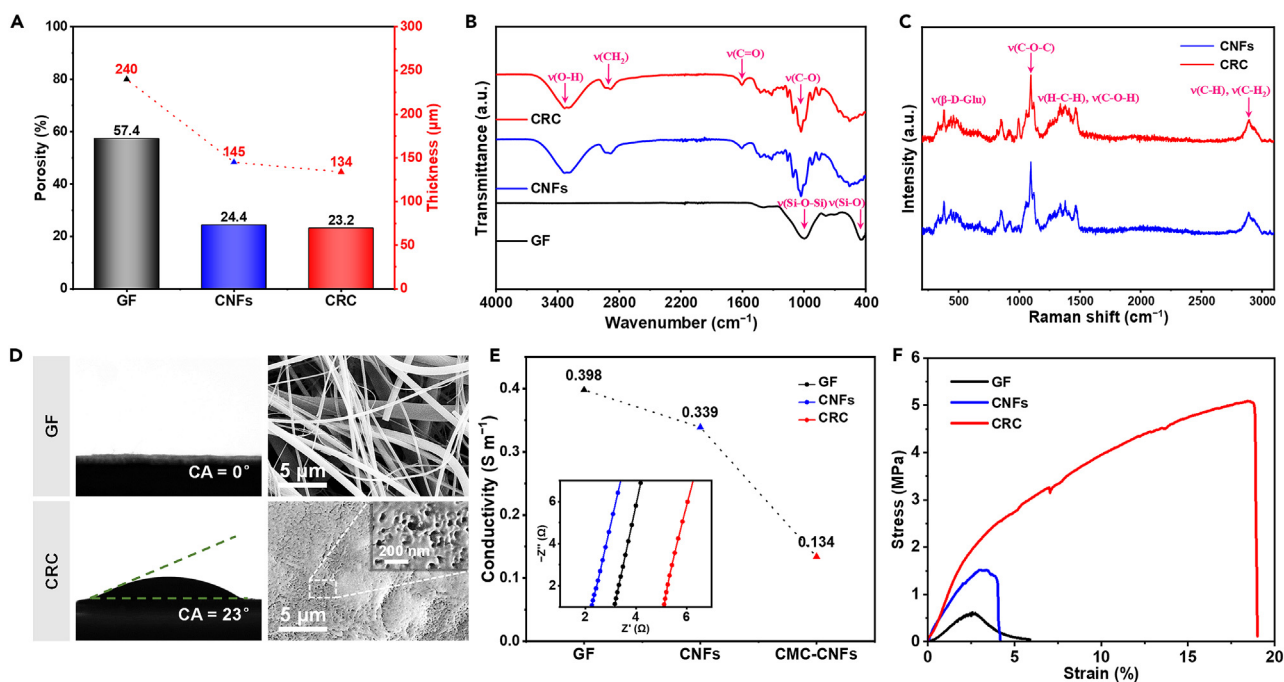
Figure 2. Physical characterization of separators
(A) Porosity and thickness.
(B) FTIR spectra.
(C) Raman spectra.
(D) Contact angle with 1 M ZnSO$_4$ electrolyte and SEM images of GF and CRC separators.
(E) Ionic conductivities and Nyquist curves of separators with 1 M ZnSO$_4$ electrolyte.
(F) Stress-strain curves of tensile characterization.

groups. Also, the high binding energy of CMC to water (Figure S3) indicates the potent hydrophilic groups in CRC separators, which contribute to limiting the reaction activity of free water molecules, thereby suppressing interfacial side reactions on the Zn anode.

The interweaving of chain segments fixes the relative position of cellulose polymers and enhances the strength and flexibility of the cellulose separator. As shown in Figure S4, CRC separators were unharmed after folding. To ensure mechanical strength while minimizing thickness for higher energy density, we need to precisely control the feeding amount during separator preparation. Ultimately, the thickness was reduced to a minimum of 134 μm, and the porosity was measured at 23.2% (Figure 2A). By adding CMC, the mechanical strength of the separator matrix can be improved due to the hydrogen bonds cross-linking and reflects on some other physical properties,[32] like the electrolyte absorption ability (Figure S5). Figure 2B reveals the chemical bonds of GF, CNFs, and CRC separators by Fourier transform infrared spectroscopy (FTIR spectroscopy). For cellulose-based separators, the characteristic peaks belong to O-H stretching and C-O stretching, proving the existence of hydrophilic hydroxyl and carboxyl groups. Figure 2C shows laser confocal Raman spectra of CNFs and CRC separators. The peaks of C-O-C and glycosidic bonds stretching vibration indicate the characteristics of separator components and the chemical connection of cellulose units. To evaluate the wettability of the separator, the contact angle measurements between 1 M ZnSO$_4$ electrolyte and different separators were adopted, as shown in Figure 2D. The drop on the GF surface is immediately absorbed for its large porosity and loose stacking. CRC separator also shows enhanced wettability with a contact angle of 23°, better than the pure CNFs separator with 30° (Figure S6). This can be attributed to more and stronger hydrophilic carboxyl groups. Enhanced wettability of the interface correlates with a decrease in the free energy of nucleation, thereby facilitating a more uniform deposition of zinc ions. The morphology of GF and CRC separators can be observed by scanning electron microscope (SEM) image, as shown in Figures 2D and S7. The loose GF filaments can create uneven surfaces that promote the nucleation of dendrites. Some detached GF filaments may migrate to the deposition layer and lead to severe dendrite growth and subsequent battery failure. In contrast, the CRC separator has a smooth surface and even pore distribution, which can lead to a uniform Zn^{2+} flux across the separator.

The ionic conductivities were measured according to the bulk resistances obtained from the Nyquist curve and the thickness of separators, calculated and shown in Figure 2E. Although the thinner thickness of the CRC separator reduces the ion transmission distance, the long-chain and stacked cellulose fibers further enhance the interaction, resulting in slower Zn^{2+} transmission in separators. The superposition of multiple factors eventually makes the ionic conductivity of all separators very close. The tensile properties of GF, CNFs, and CRC separators were measured by electro-mechanical universal testing machines as shown in Figure 2F. The results show that the tensile strength of CRC separator increased by 733% (5.08 MPa) than that of the GF separator (0.61 MPa). This can be attributed to the cross-linking of hydrogen bonds between CNFs and CMC. It also can be found that the maximum elongation of the CRC separator is greatly improved, reaching 18%, much more than
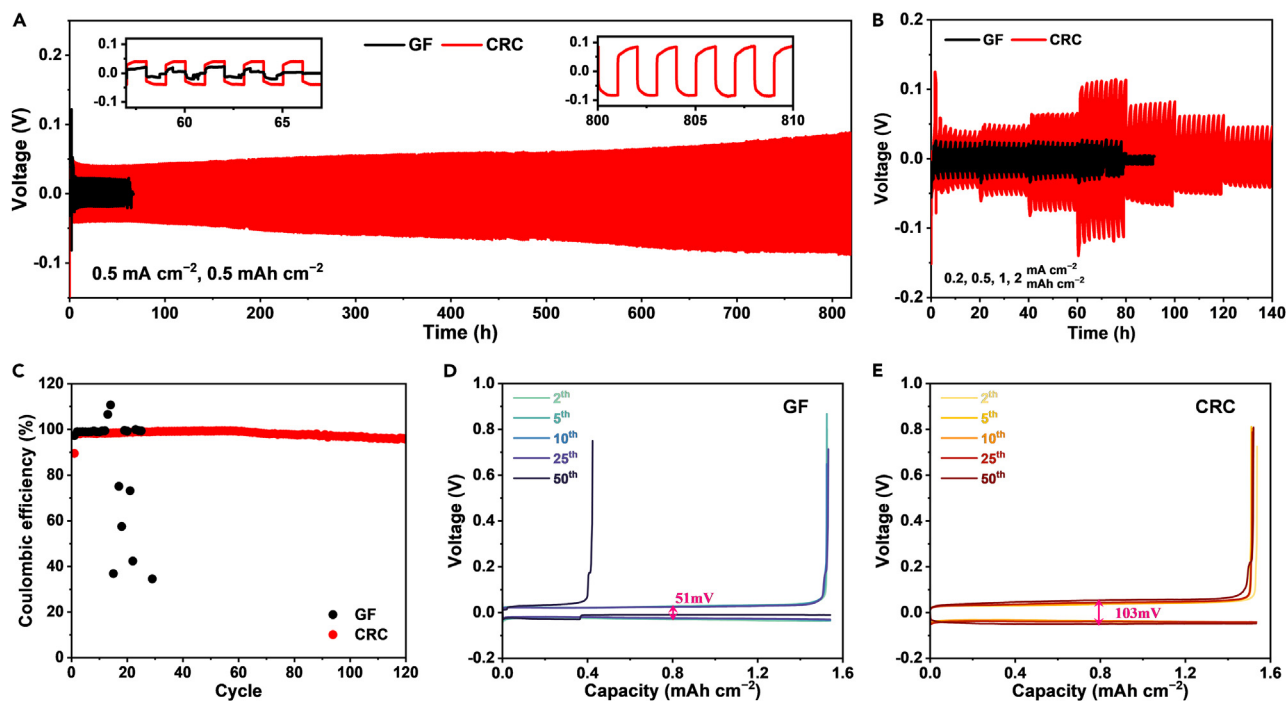
Figure 3. Analyses of electrochemical performances of symmetric cells and half cells
(A) Cycling performances of Zn||Zn cells with GF and CRC separators.
(B) Rate performances of Zn||Zn cells with GF and CRC separators.
(C) Column efficiency of Zn||Cu cells with GF and CRC separators.
(D and E) GCD profiles for selected cycles of Zn||Cu cells with (D) GF and (E) CRC separators.

the elongation of CNFs (3%) and GF separators (2.5%). The increasing mechanical strength of the CRC separator will resist the puncture of Zn dendrites and inhibit further dendrite growth.

Electrochemical performance of symmetric cells and half cells

The electrochemical performances of Zn anodes can be evaluated by Zn||Zn symmetric cells with GF and CRC separators. Initially, the properties of separators were optimized by the cycling performances of Zn||Zn cells (Figures S8 and S9). The cycling lifespan of zinc anodes was improved with the incorporation of CMC for the strong zinc-philic groups, which will lead to a more uniform deposition of Zn^{2+}. After the determination of optimal ratio and thickness, assembled Zn||Zn symmetric cells were tested at a current density of 0.5 mA cm^{-2} and an areal capacity of 0.5 mAh cm^{-2} (Figure 3A). The cell assembled with GF separator short-circuited after 50 h, while the cell with CRC separator cycled stably for more than 800 h, which is superb compared to previously reported works (Table S1). In addition, the cell with CRC separator can be cycled stably for a long time under larger current density and higher capacity, as shown in Figure S10. The results can be explained by the greatly enhanced mechanical properties, resisting the puncture of dendrites. Meanwhile, DFT calculation results prove that the polyanionic structure of CRC separators can interact with Zn^{2+} and enable uniform Zn^{2+} deposition, thus exhibiting a stable Zn anode. The rate performances of Zn||Zn cells were tested at various current densities ranging from 0.2 mA cm^{-2} and 0.2 mAh cm^{-2} to 2 mA cm^{-2} and 2 mAh cm^{-2}, as shown in Figure 3B. The cell with GF separator short-circuited after 80 h for the increase of current density, while the cell with CRC separator maintained excellent cycle reversibility. Before and after the stable 140 h cycling, the corresponding polarization voltage of the cell did not differ much, indicating that the CRC separator exhibits excellent rate capability and cycle stability.

To further study the influence of separators on plating/stripping reversibility, Zn||Cu half cells with GF and CRC separators were assembled and tested at a current density of 1 mA cm^{-2} and a capacity of 1 mAh cm^{-2}. As shown in Figure 3C, the coulombic efficiency of the cell with the GF separator fluctuated sharply and decreased rapidly after 20 cycles. Such violent fluctuation means battery failure. In contrast, the CRC separator maintained a high average coulombic efficiency of 98.04% after 120 cycles, showing improved reversibility of the plating/stripping behavior of Zn^{2+}. Meanwhile, the nucleation overpotential can be analyzed from galvanostatic charge/discharge (GCD) profiles, as shown in Figures 3D and 3E. The nucleation overpotential of the cell with the CRC separator had a slight increase during the cycling process and remained at 103 mV after 50 cycles, while the nucleation overpotential of the GF separator stayed at 51 mV. The increase of nucleation overpotential of CRC separator can also be analyzed from the cyclic voltammetry (CV) curves of Zn||SS half cells (Figure S11). Both qualitative analyses reflect better Zn^{2+} deposition behavior. Furthermore, a large nucleation overpotential will decrease the radius of nuclei, increase the number of active sites, and ultimately lead to a more uniform Zn^{2+} deposition.
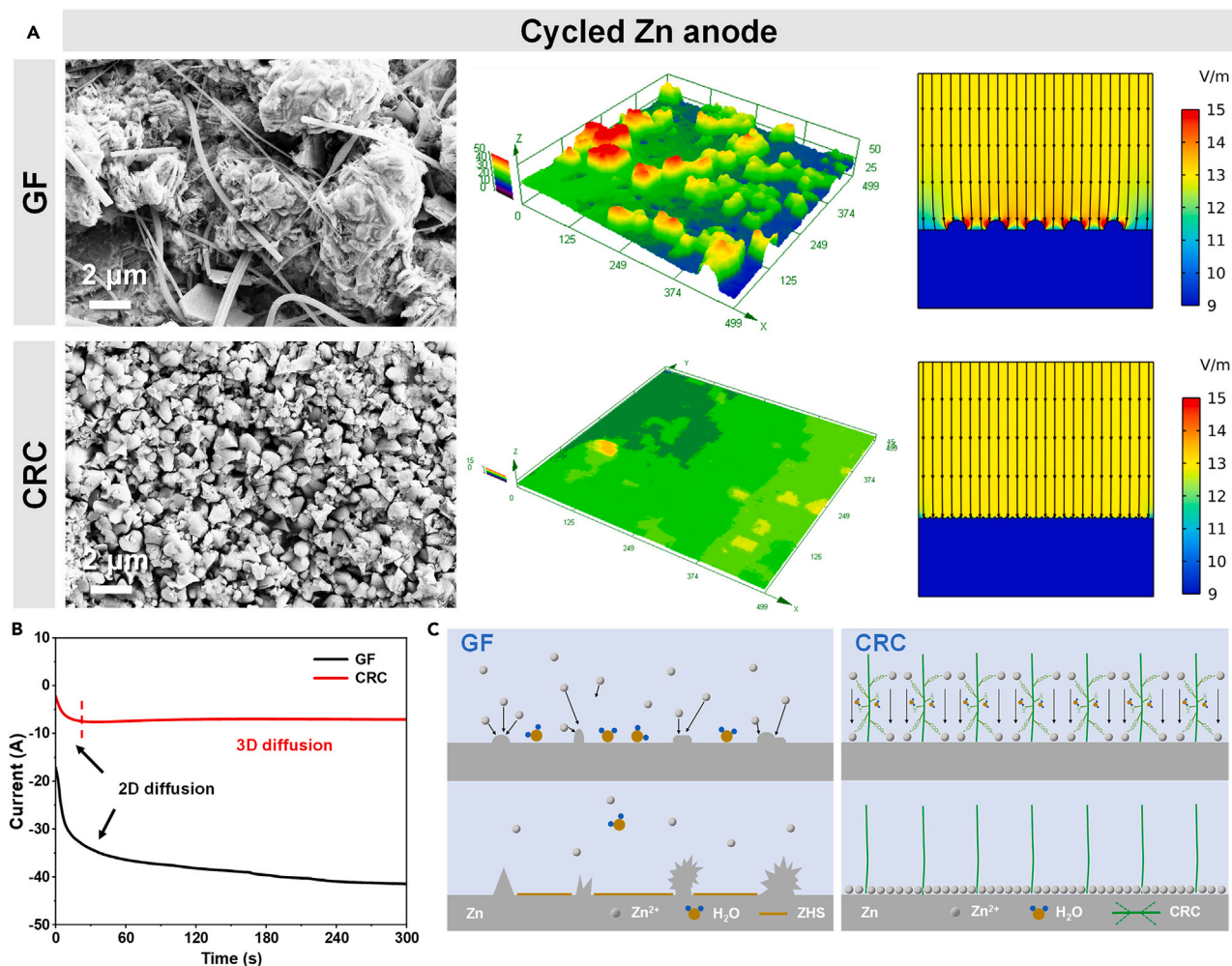
Figure 4. Characterization of Zn²⁺ deposition behavior with GF and CRC separators
(A) SEM, CLSM, and COMSOL simulations images of Zn anode after 25 cycles.
(B) CA curves under an overpotential of −150 mV.
(C) Schematic illustration of Zn²⁺ deposition behaviors.

Improvement of Zn²⁺ deposition and side reaction inhibition

The surface morphology of the Zn anode of the Zn∥Zn cells with GF and CRC separators was observed by SEM and confocal laser scanning microscope (CLSM) images, as shown in Figure 4A. After 25 cycles, the Zn anode of the cell with the GF separator has obvious dendrite on the Zn deposited surface, while the cell with the CRC separator has homogeneous deposition with a unique pyramidal morphology. The results signify the total importance of the CRC separator for promoting even Zn deposition. Meanwhile, the uniform deposition of cycled anodes and the integrity of cycled separators (Figures S12 and S13) show nearly no dead Zn, indicating reversible and uniform Zn²⁺ distribution. In contrast, the GF filaments detached from the separator can be monitored in the deposition layer, which will cause much more uneven electric field distribution on the Zn anode. The relationship between the deposition planeness and the electric field distribution can be simulated by COMSOL Multiphysics software, as shown in Figure 4A. The simulation results indicate that uneven Zn²⁺ deposition will lead to uneven electric field distribution on the Zn anode with a GF separator. Simultaneously, Zn²⁺ are guided by the electric field to deposit at the lowest potential position. For uneven electric field area, the lowest potential position is the tip of the dendrites. The deposition phenomenon is the so-called "tip effect." Conversely, uniform Zn²⁺ distribution and abundant zinc-philic groups of CRC separator will guide regular electric field configuration and regular deposition. The results of SEM, SLSM, and COMSOL simulation jointly suggest that CRC separators can inhibit the "tip effect," resulting in dendrites-free Zn anodes and stable cycling performances.

The nucleation process has an important significance for the morphology evolution of Zn deposition in the later stage, which can be verified by the chronoamperometry (CA) test. The increase of effective surface area will lead to the increase of current. Zn²⁺ tends to diffuse laterally along the Zn surface, and the aggregation of Zn atoms to form large particles is a favorable way to minimize the surface energy. As shown
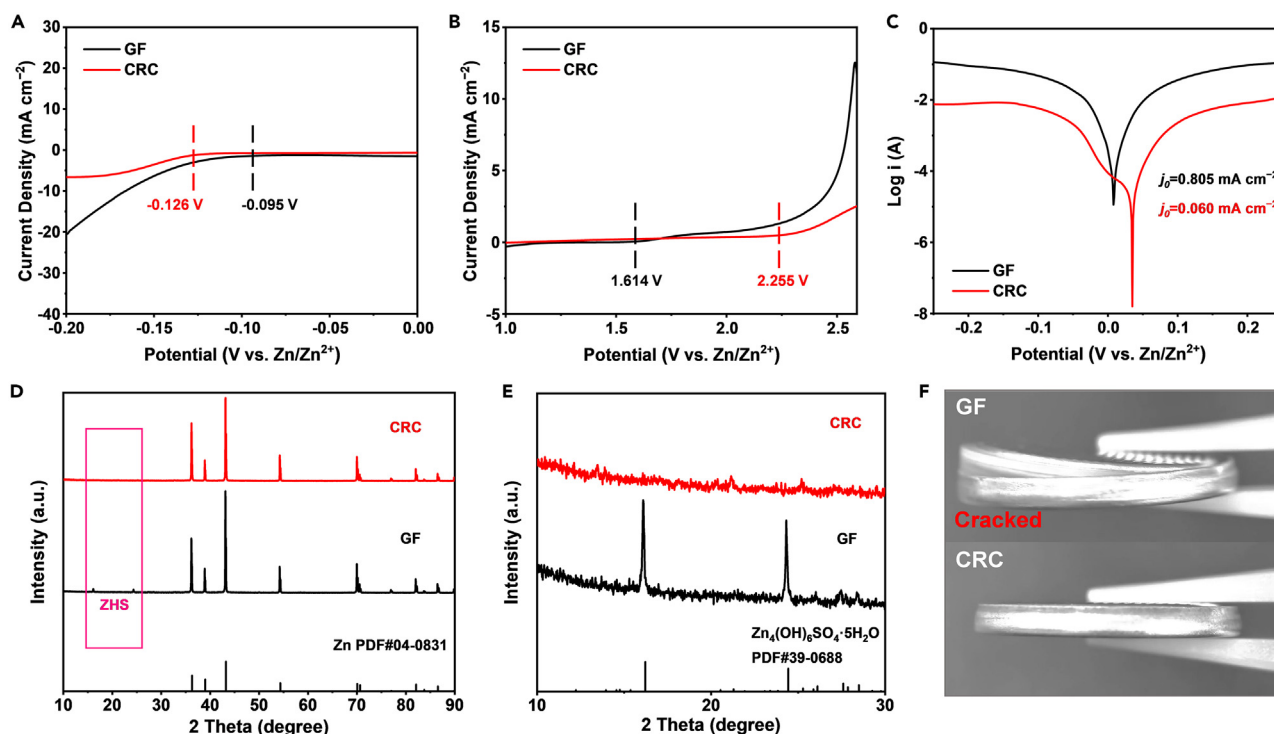
Figure 5. Regulation of side reactions on Zn anode
(A and B) LSV curves with GF and CRC separators.
(C) Tafel curves with GF and CRC separators.
(D and E) (D) Full view and (E) magnified view from XRD patterns of Zn anodes after 25 cycles.
(F) Optical photos of cells after large current cycling.

in Figure 4B, under an overpotential of -150 mV, the increase of current density in the initial stage represents the nucleation process of Zn^{2+}. The cell with GF separator has a continuous increase of current density, indicating the effective anode area increases. The cell with CRC separator only increases for 50 s until reaching the stable current density, indicating that the 3D diffusion dominates the deposition behavior. To investigate the ion transport regulation of separators, the Zn^{2+} transfer number measurements are tested and calculated ($t_{Zn}^{2+} = 0.32$) in Zn symmetric cells (Figure S14). Figure 4C shows the schematic illustration of Zn deposition behavior with different separators. Compared with the GF separator with large and uneven pore size, the CRC separator relies on the cellulose chain segments to guide the uniform deposition of Zn^{2+}, which can avoid the formation of dendrites. In summary, the morphology images, COMSOL simulation, and CA test results jointly illustrate this outcome-oriented function, inhibiting the growth of Zn dendrites and resulting in stable and reversible Zn anodes.

The side reactions on the Zn anode during cycling were further studied by linear sweep voltammetry (LSV) and Tafel test results. As shown in Figures 5A and 5B, in sweep processes, the electrochemical stability window of the cell with CRC separator (-0.126 V–2.255 V) is much broader than that of the cell with GF separator (-0.095 V–1.614 V), proving that CRC separator can suppress the hydrogen and oxygen evolution side reactions on the Zn anode. As shown in Figure 5F, if the gas generation during long-time cycling (50 cycles under 5 mA cm^{-2} and 5 mAh cm^{-2}) is not suppressed, the cell will crack due to the increase in pressure. Otherwise, the cell with CRC separator sustained a long cycling life. The results of the Tafel test are shown in Figure 5C. The Tafel plots further confirm the inhibitory effect of the CRC separator on Zn anode corrosion. The corrosion current density (j_0) of the Zn anode with the CRC separator (0.060 mA cm^{-2}) is much lower than that with the GF separator (0.805 mA cm^{-2}). Figures 5D and 5E show the X-ray diffraction (XRD) patterns of the Zn anode after 25 cycles. The boxed area is the diffraction angle region of passivation products. The XRD pattern of the Zn anode with the CRC separator shows no characteristic peaks of ZHS. Therefore, it confirms that the CRC separator can effectively inhibit the formation of passivation products. It may, due to the abundant hydrophilic groups in CRC separators, firmly trap water molecules by hydrogen bonds, reducing the reaction activity of water molecules on the Zn anode. The results indicate a reversible Zn anode contributed by CRC separators, which can alleviate the issues of passivation, corrosion, and other side reactions in AZIBs.

Electrochemical performance of full cells

Vanadium dioxide (VO_2) has a typical tunnel structure, which exhibits fast cation diffusion, higher capacity, and superior rate capability than other vanadium oxides, making it a suitable energy storage cathode material. Figure 6A shows the SEM image of pure-phase VO_2 prepared by a hydrothermal method. The prepared VO_2 has a typical 2D nanobelt structure, which facilitates the contact between the cathode and the
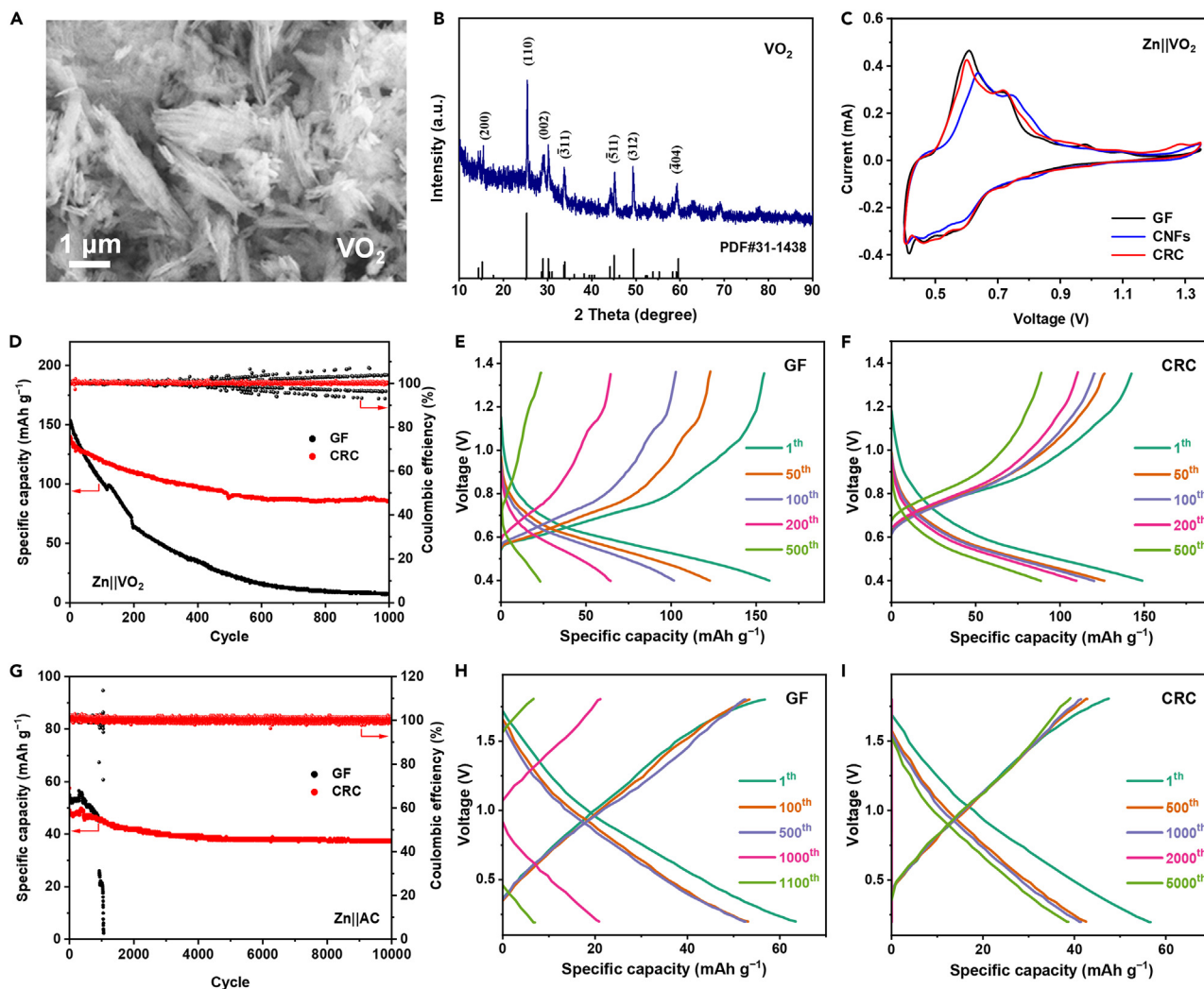
Figure 6. Analyses of cathode and electrochemical performance of full cells
(A) SEM images of synthesized VO_2.
(B) XRD patterns of synthesized VO_2.
(C) CV profiles at the second cycle of $Zn\|VO_2$ cells with GF, CNFs, and CRC separators.
(D) Cycling performance of $Zn\|VO_2$ cells at 1 A g^{-1}.
(E and F) Charge/discharge profiles of $Zn\|VO_2$ cells with (E) GF and (F) CRC separators.
(G) Cycling performance of $Zn\|AC$ cells at 1 A g^{-1}.
(H and I) Charge/discharge profiles of $Zn\|AC$ cells with (H) GF and (I) CRC separators.

electrolyte. Meanwhile, XRD analysis of the prepared VO_2 was performed (Figure 6B) to confirm that its crystal structure matches expectations. $Zn\|VO_2$ cells were assembled with GF and CRC separators, respectively. The CV profiles of $Zn\|VO_2$ cells are shown in Figure 6C. The scanning window range is from 0.4 V to 1.35 V (vs. Zn^{2+}/Zn), at a scan rate of 0.1 mV s^{-1}. Multiple reduction and oxidation peaks appear in the sweep process, indicating reversible multi-step insertion and extraction of Zn^{2+} in the cathode. The CV curve of the cell with CRC separator is broader, suggesting great electrochemical performance. The cycling performances of $Zn\|VO_2$ cells with GF and CRC separators at 1 A g^{-1} are shown in Figure 6D. The specific discharge capacity with the GF separator rapidly decayed to 50% after 200 cycles, and the coulombic efficiency fluctuated heavily, indicating that the battery had failed. By contrast, the cell with CRC separator maintained a capacity retention rate of 61.87% after 1,000 cycles with an initial capacity of 140 mAh g^{-1}, and the coulombic efficiency remained at almost 100%, showing the excellent cycle stability of CRC separators. The charge/discharge profiles of $Zn\|VO_2$ cells are shown in Figures 6E and 6F. The rapid capacity decrease observed with GF separators suggests a swift failure of the cathode material, often attributed to the degradation or dissolution of VO_2. In contrast, the cell with CRC separators maintains a high capacity after long cycling, thus suggesting that CRC separators exhibit the ability to inhibit the degradation or dissolution of VO_2.
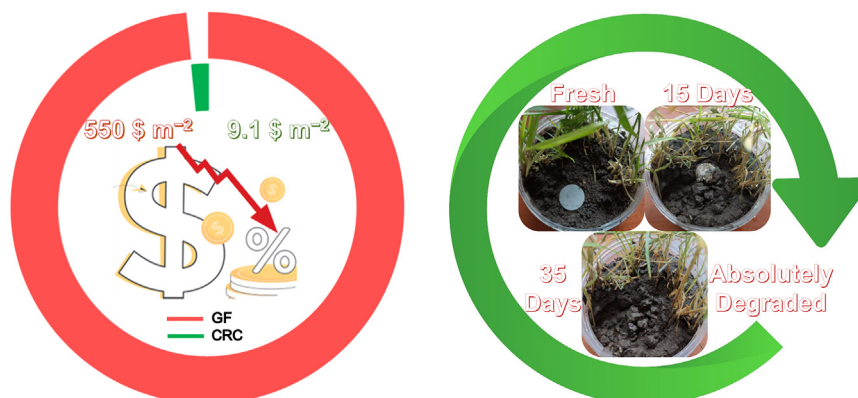
Figure 7. Contrast on cost and degradability of separators

Activated carbon (AC) as a cathode material is commonly used in aqueous zinc-ion capacitors (AZICs) for high conductivity, low cost, and greenness. To explore the potential of CRC separators in AZICs, Zn||AC capacitors were assembled with commercial AC products. The cycling performances were tested at a current density of 1 A g^{-1}, as shown in Figure 6G. The discharge capacity of the Zn||AC cell assembled with the GF separator tended to zero after 1,100 cycles for short circuit. In comparison, the Zn||AC cell with the CRC separator reached an initial capacity of 58 mAh g^{-1}, a final capacity retention rate of 65.52%, and a coulombic efficiency at almost 100% after 10,000 cycles. Figures 6H and 6I show the charge/discharge profiles of Zn||AC capacitors. The results indicate that the CRC separator achieves superior reversibility of Zn anodes. The rate capacities of Zn||VO$_2$ and of Zn||AC cells were tested and shown in Figure S15. All results show the excellent cycle stability of CRC separators in AZIBs and the ability to match multiple cathode materials.

Discussion of practical advantages

As an alternative energy storage solution, the practical implementation of AZIBs necessitates cost-effectiveness and environmental friendliness.[18,19] Considering adequate cycling performance, this work introduces the crucial aspects of cost and degradability. In practical applications, CRC separators are highlighted as markedly economical, and eco-friendly, especially compared with the most commonly used commercial GF and other separators.[18,19,33–35] Tables S2 and S3 list the comparison of related works containing the discussion of cost and degradability. As shown in Figure 7, the bulk pricing of commercial GF separators approaches almost 550 $ m^{-2}. In contrast, the area cost of CRC separators is at a very low price about 9.1 $ m^{-2} accounting for all source materials. The significant cost advantage provides a viable option for practical applications of battery separators. Furthermore, Figure 7 shows the nature-degradable properties of CRC separators. After being exposed to earth, the bio-based CRC separator gradually degraded after 35 days, confirming the impressive environmental benignity of the construct.

Conclusions

In summary, the CRC separators were obtained all from cellulose derivatives. The significantly improved mechanical properties of the separator inhibit the Zn anode from dendrite growth. The zinc-philic groups facilitate better binding to Zn^{2+}, resulting in uniform nucleation and deposition. Also, abundant hydrophilic groups can trap water molecules to inhibit the occurrence of side reactions. A stable cycle of Zn||Zn cell exceeded 800 h under 0.5 mA cm^{-2} and 0.5 mAh cm^{-2}, and the average coulomb efficiency of Zn||Cu cell reached 98.04% after 120 cycles. Assembled full cells with CRC separators also show excellent electrochemical performances. Zn||VO$_2$ full cells exhibited an initial capacity of 140 mAh g^{-1} at 1 A g^{-1} and a capacity retention rate of 61.87% after 1,000 cycles. The Zn||AC capacitors exhibited an initial capacity of 58 mAh g^{-1} at 1 A g^{-1} and a capacity retention rate of 65.52% after 10,000 cycles. The coulombic efficiency maintained at almost 100%. This work paves a novel path for exploring economical and eco-friendly battery separators to achieve stable Zn anode and high-performance AZIBs.

Limitations of the study

After the determination of the optimal ratio, the thickness of CRC separators is at a level of about 100 μm. This is due to the simple sol-gel methods with tap casting and dehydration processes, which cost very little but still have potential to reduce the thickness. For further in-depth study, more advanced techniques, such as roll-to-roll coating and single-screw extrusion, should be introduced to the craft of modified CNFs sheets for the control of thickness parameters. In addition, the performance of the CRC separators should be studied using assembled pouch cells as opposed to coin cells.

STAR★METHODS

Detailed methods are provided in the online version of this paper and include the following:

- KEY RESOURCES TABLE

- RESOURCE AVAILABILITY
  - Lead contact
  - Materials availability
  - Data and code availability
- METHOD DETAILS
  - Preparation of separators
  - Preparation of cathodes
  - Characterizations
  - Electrochemical measurements
  - Calculation method
  - Simulation method

SUPPLEMENTAL INFORMATION

Supplemental information can be found online at https://doi.org/10.1016/j.isci.2024.110237.

AUTHOR CONTRIBUTIONS

H.Z. conceived the project, designed the experiments, and wrote the manuscript. H.Z. and J.L. prepared materials and performed measurements. H.R., J.W., and Y.G. helped with the characterization and discussion. B.W., D.W., H.L., and S.D. revised and finalized the manuscript.

DECLARATION OF INTERESTS

The authors declare no competing interests.

REFERENCES

1. Gourley, S.W., Brown, R., Adams, B.D., and Higgins, D. (2023). Zinc-ion batteries for stationary energy storage. Joule 7, 1415–1436. https://doi.org/10.1016/j.joule.2023.06.007.

2. Zampardi, G., and La Mantia, F. (2022). Open challenges and good experimental practices in the research field of aqueous Zn-ion batteries. Nat. Commun. 13, 687. https://doi.org/10.1038/s41467-022-28381-x.

3. Liu, S., Zhang, R., Wang, C., Mao, j., Chao, D., Zhang, C., Zhang, S., and Guo, Z. (2024). Zinc ion Batteries: Bridging the Gap from Academia to Industry for Grid-Scale Energy Storage. Angew. Chem. Int. Ed. 63, e202400045. https://doi.org/10.1002/anie.202400045.

4. Yi, Z., Chen, G., Hou, F., Wang, L., and Liang, J. (2021). Strategies for the Stabilization of Zn Metal Anodes for Zn-Ion Batteries. Adv. Energy Mater. 11, 2003065. https://doi.org/10.1002/aenm.202003065.

5. Li, M., Li, Z., Wang, X., Meng, J., Liu, X., Wu, B., Han, C., and Mai, L. (2021). Comprehensive understanding of the roles of water molecules in aqueous Zn-ion batteries: from electrolytes to electrode materials. Energy Environ. Sci. 14, 3796–3839. https://doi.org/10.1039/D1EE00030F.

6. Ren, H., Li, S., Wang, B., Gong, Y., Zhang, H., Wang, J., Lv, Q., Wang, D., Liu, H., and Dou, S. (2024). Mapping the design of electrolyte additive for stabilizing zinc anode in aqueous zinc ion batteries. Energy Storage Mater. 68, 103364. https://doi.org/10.1016/j.ensm.2024.103364.

7. Gong, Y., Wang, B., Ren, H., Li, D., Wang, D., Liu, H., and Dou, S. (2023). Recent Advances in Structural Optimization and Surface Modification on Current Collectors for High-Performance Zinc Anode: Principles, Strategies, and Challenges. Nano-Micro Lett. 15, 208. https://doi.org/10.1007/s40820-023-01177-4.

8. Lagadec, M.F., Zahn, R., and Wood, V. (2018). Characterization and performance evaluation of lithium-ion battery separators. Nat. Energy 4, 16–25. https://doi.org/10.1038/s41560-018-0295-9.

9. Zong, Y., He, H., Wang, Y., Wu, M., Ren, X., Bai, Z., Wang, N., Ning, X., and Dou, S.X. (2023). Functionalized Separator Strategies toward Advanced Aqueous Zinc-Ion Batteries. Adv. Energy Mater. 13, 2300403. https://doi.org/10.1002/aenm.202300403.

10. Ruan, P., Liang, S., Lu, B., Fan, H.J., and Zhou, J. (2022). Design Strategies for High-Energy-Density Aqueous Zinc Batteries. Angew.

Chem. Int. Ed. 61, e202200598. https://doi.org/10.1002/anie.202200598.

11. Ma, L., Chen, R., Hu, Y., Zhang, W., Zhu, G., Zhao, P., Chen, T., Wang, C., Yan, W., Wang, Y., et al. (2018). Nanoporous and lyophilic battery separator from regenerated eggshell membrane with effective suppression of dendritic lithium growth. Energy Storage Mater. 14, 258–266. https://doi.org/10.1016/j.ensm.2018.04.016.

12. Hao, Z., Dai, Y., Xu, X., Zhao, X., Cong, Y., Wu, X., and Zhou, W. (2023). Strategies for addressing the challenges of aqueous zinc batteries enabled by functional separators. J. Mater. Chem. A 11, 11031–11047. https://doi.org/10.1039/D3TA01706K.

13. Ren, H., Li, S., Wang, B., Zhang, Y., Wang, T., Lv, Q., Zhang, X., Wang, L., Han, X., Jin, F., et al. (2023). Molecular-Crowding Effect Mimicking Cold-Resistant Plants to Stabilize the Zinc Anode with Wider Service Temperature Range. Adv. Mater. 35, 2208237. https://doi.org/10.1002/adma.202208237.

14. Wang, Z., Lee, Y.-H., Kim, S.-W., Seo, J.-Y., Lee, S.-Y., and Nyholm, L. (2021). Why Cellulose-Based Electrochemical Energy Storage Devices? Adv. Mater. 33, 2000892. https://doi.org/10.1002/adma.202000892.

15. Ferro, M., Mannu, A., Panzeri, W., Theeuwen, C.H.J., and Mele, A. (2020). An Integrated Approach to Optimizing Cellulose Mercerization. Polymers 12, 1559. https://doi.org/10.3390/polym12071559.

16. Popescu, M.-C., Dogaru, B.-I., and Popescu, C.-M. (2020). Effect of Cellulose Nanocrystals Nanofiller on the Structure and Sorption Properties of Carboxymethyl Cellulose–Glycerol–Cellulose Nanocrystals Nanocomposite Systems. Materials 13, 2900. https://doi.org/10.3390/ma13132900.

17. Li, Z., Ye, L., Zhou, G., Xu, W., Zhao, K., Zhang, X., Hong, S., Ma, T., Li, M.-C., Liu, C., and Mei, C. (2023). A water-gating and zinc-sieving lignocellulose nanofiber separator for dendrite-free rechargeable aqueous zinc ion battery. Chem. Eng. J. 457, 141160. https://doi.org/10.1016/j.cej.2022.141160.

18. Cao, J., Zhang, D., Chanajaree, R., Luo, D., Yang, X., Zhang, X., and Qin, J. (2024). A low-cost separator enables a highly stable zinc anode by accelerating the de-solvation effect. Chem. Eng. J. 480, 147980. https://doi.org/10.1016/j.cej.2023.147980.

19. Zhang, Y., Li, X., Fan, L., Shuai, Y., and Zhang, N. (2022). Ultrathin and super-tough membrane for anti-dendrite separator in aqueous zinc-ion batteries. Cell Rep. Phys. Sci. 3, 100824. https://doi.org/10.1016/j.xcrp.2022.100824.

20. Yang, S., Zhang, Y., Zhang, Y., Deng, J., Chen, N., Xie, S., Ma, Y., and Wang, Z. (2023). Designing Anti-Swelling Nanocellulose Separators with Stable and Fast Ion Transport Channels for Efficient Aqueous Zinc-Ion Batteries. Adv. Funct. Mater. 33, 2304280. https://doi.org/10.1002/adfm.202304280.

21. Li, C., Sun, Z., Yang, T., Yu, L., Wei, N., Tian, Z., Cai, J., Lv, J., Shao, Y., Rümmeli, M.H., et al. (2020). Directly Grown Vertical Graphene Carpets as Janus Separators toward Stabilized Zn Metal Anodes. Adv. Mater. 32, 2003425. https://doi.org/10.1002/adma.202003425.

22. Fang, Y., Xie, X., Zhang, B., Chai, Y., Lu, B., Liu, M., Zhou, J., and Liang, S. (2022). Regulating Zinc Deposition Behaviors by the Conditioner of PAN Separator for Zinc-Ion Batteries. Adv. Funct. Mater. 32, 2109671. https://doi.org/10.1002/adfm.202109671.

23. Wang, Z., Dong, L., Huang, W., Jia, H., Zhao, Q., Wang, Y., Fei, B., and Pan, F. (2021). Simultaneously Regulating Uniform Zn^{2+} Flux and Electron Conduction by MOF/rGO Interlayers for High-Performance Zn Anodes. Nano-Micro Lett. 13, 73. https://doi.org/10.1007/s40820-021-00594-7.

24. Ge, X., Zhang, W., Song, F., Xie, B., Li, J., Wang, J., Wang, X., Zhao, J., and Cui, G. (2022). Single-Ion-Functionalized Nanocellulose Membranes Enable Lean-Electrolyte and Deeply Cycled Aqueous Zinc-Metal Batteries. Adv. Funct. Mater. 32, 2200429. https://doi.org/10.1002/adfm.202200429.

25. Liu, Y., Liu, S., Xie, X., Li, Z., Wang, P., Lu, B., Liang, S., Tang, Y., and Zhou, J. (2023). A functionalized separator enables dendrite-free Zn anode via metal-polydopamine coordination chemistry. InfoMat 5, e12374. https://doi.org/10.1002/inf2.12374.

26. Zhou, W., Chen, M., Tian, Q., Chen, J., Xu, X., and Wong, C.-P. (2022). Cotton-derived cellulose film as a dendrite-inhibiting separator to stabilize the zinc metal anode of aqueous zinc ion batteries. Energy Storage Mater. 44, 57–65. https://doi.org/10.1016/j.ensm.2021.10.002.

27. Fu, J., Wang, H., Xiao, P., Zeng, C., Sun, Q., and Li, H. (2022). A high strength, anti-corrosion and sustainable separator for aqueous zinc-based battery by natural bamboo cellulose. Energy Storage Mater. 48, 191–191.f6. https://doi.org/10.1016/j.ensm.2022.02.052.

28. Xi, C., Xiao, Y., Yang, C., Li, M., Li, L., Chao, Y., Li, L., He, C., and Yu, Y. (2023). Localized gelation cellulose separators enable dendrite-free anodes for future zinc-ion batteries. J. Mater. Chem. A 11, 6522–6529. https://doi.org/10.1039/D3TA00094J.

29. Sun, Y.-Y., Yan, L., Zhang, Q., Wang, T.-B., Zha, Y.-C., Fan, L., and Jiang, H.-F. (2023). Mixed cellulose ester membrane as an ion redistributor to stabilize zinc anode in aqueous zinc ion batteries. J. Colloid Interface Sci. 641, 610–618. https://doi.org/10.1016/j.jcis.2023.03.079.

30. Xu, L., Meng, T., Zheng, X., Li, T., Brozena, A.H., Mao, Y., Zhang, Q., Clifford, B.C., Rao, J., and Hu, L. (2023). Nanocellulose-Carboxymethylcellulose Electrolyte for Stable, High-Rate Zinc-Ion Batteries. Adv. Funct. Mater. 33, 2302098. https://doi.org/10.1002/adfm.202302098.

31. Wei, J., Jia, S., Zhang, L., Zhou, Y., Lv, Y., Zhang, X., and Shao, Z. (2021). Preparation of treelike and rodlike carboxymethylated nanocellulose and their effect on carboxymethyl cellulose films. J. Appl. Polym. Sci. 138, 50092. https://doi.org/10.1002/app.50092.

32. Zhang, Y., Yang, G., Lehmann, M.L., Wu, C., Zhao, L., Saito, T., Liang, Y., Nanda, J., and Yao, Y. (2021). Separator Effect on Zinc Electrodeposition Behavior and Its Implication for Zinc Battery Lifetime. Nano Lett. 21, 10446–10452. https://doi.org/10.1021/acs.nanolett.1c03792.

33. Aeby, X., Poulin, A., Siqueira, G., Hausmann, M.K., and Nyström, G. (2021). Fully 3D Printed and Disposable Paper Supercapacitors. Adv. Mater. 33, 2101328. https://doi.org/10.1002/adma.202101328.

34. Mittal, N., Ojanguren, A., Kundu, D., Lizundia, E., and Niederberger, M. (2023). Bottom-Up Design of a Green and Transient Zinc-Ion Battery with Ultralong Lifespan. Small 19, 2206249. https://doi.org/10.1002/smll.202206249.

35. Liu, A., Jiang, Z., Li, S., Du, J., Tao, Y., Lu, J., Cheng, Y., and Wang, H. (2022). A degradable membrane based on lignin-containing cellulose for high-energy lithium-ion batteries. Int. J. Biol. Macromol. 213, 690–698. https://doi.org/10.1016/j.ijbiomac.2022.06.004.

36. Perdew, J.P., Burke, K., and Ernzerhof, M. (1996). Generalized Gradient Approximation Made Simple. Phys. Rev. Lett. 77, 3865–3868. https://doi.org/10.1103/PhysRevLett.77.3865.

37. Delley, B. (1990). An all-electron numerical method for solving the local density functional for polyatomic molecules. J. Chem. Phys. 92, 508–517. https://doi.org/10.1063/1.458452.

38. Delley, B. (2000). From molecules to solids with the DMol3 approach. J. Chem. Phys. 113, 7756–7764. https://doi.org/10.1063/1.1316015.

39. Grimme, S., Antony, J., Ehrlich, S., and Krieg, H. (2010). A consistent and accurate ab initio parametrization of density functional dispersion correction (DFT-D) for the 94 elements H-Pu. J. Chem. Phys. 132, 154104. https://doi.org/10.1063/1.3382344.

STAR★METHODS

KEY RESOURCES TABLE

REAGENT or RESOURCE	SOURCE	IDENTIFIER
Chemicals, peptides, and recombinant proteins		
Cellulose nanofibers	NanoFC	CAS: 9004-34-6
Carboxymethyl cellulose	Macklin	CAS: 9004-32-4
Zinc sulfate heptahydrate	Aladdin	CAS: 7446-20-0
Vanadium pentoxide	Aladdin	CAS: 1314-62-1
Activated carbon	XFNANO	CAS: 7440-44-0
Deposited data		
Cost statistics of commercial separators	https://doi.org/10.1016/j.xcrp.2022.100824	N/A

RESOURCE AVAILABILITY

Lead contact

Further information and requests for resources and reagents should be directed to and will be fulfilled by the lead contact, Bo Wang (wangbo19880804@163.com).

Materials availability

This study did not generate new unique reagents.

Data and code availability

- All data reported in this paper will be shared by the lead contact upon request.
- This paper does not report original code.
- Any additional information required to reanalyze the data reported in this paper is available from the lead contact upon request.

METHOD DETAILS

Preparation of separators

The CRC separator was synthesized via a sol-gel method with tap casting and dehydration processes. Briefly, 0.05 g of sodium carboxymethyl cellulose (CMC) and 7 g of deionized water were mixed and stirred for uniform dispersion. Then add 8 g of 2.5 wt% cellulose nanofibers (CNFs) dispersion and 0.3 g of glycerol into it, and seal it immediately. The solution will be stirred for 9 h at room temperature, and then homogenized by ultrasonic homogenizer. Vacuum the gel-like solution for 5 min to remove the air bubbles, and pour it into a round plastic dish with a diameter of 60 mm. Then, the mixed solution was dried at 50°C for 8 h in the oven. Finally, the CRC separator was obtained. For comparison, the pure CNFs separator and CRC separators with various CMC addition was prepared under the same condition, respectively.

Preparation of cathodes

The VO_2 cathode was prepared via a hydrothermal reaction. Typically, 182 mg of commercial V_2O_5 powder was dispersed into the solution containing 198 mg of glucose and 70 mL of deionized water with stirring. The mixed solution was transferred into a 100 mL stainless steel autoclave and maintained at 180°C for 10 h. After cooling to room temperature naturally, the products were collected and washed with deionized water, then dried in a vacuum at 80°C for 12 h. The VO_2 powder was obtained by grinding the dried VO_2 lump. VO_2 cathodes were prepared by mixing the VO_2, Super P, and PVDF in a mass ratio of 7:2:1, dispersed in NMP to form a uniform mud. The VO_2 slurry was coated onto the surface of Ti foil, and the electrodes were dried at 60°C under vacuum for 12 h. Active carbon (AC) cathodes were prepared in the same manner in a mass ratio of 8:1:1. The mass loading of both cathodes was about 1.5-2.5 mg cm^{-2}.

Characterizations

The morphologies of Zn anodes and cathode materials were collected by scanning electron microscopy (SEM) on ZEISS-SUPRA55. The morphologies of separator components were collected by transmission electron microscopy (TEM) on FEI Talos F200X. Confocal laser scanning microscope (CLSM) images were obtained by Olympus-OLS3000. The crystallographic data of samples were recorded by X-ray diffraction (XRD) on Bruker-D2 Advance. Fourier transform infrared (FT-IR) were gathered by Thermo Fisher Scientific-Nicolet is50. Raman spectroscopy

was obtained by Renishaw-in Via-Reflex using a 785 nm diode-pumped solid-state laser. The porosity of different separators was measured by *n*-butanol immersion method, and calculated according to the below equation:

$$Porosity\ (\%)\ =\ (\Delta m\ /\ \rho)/V_0 \times 100\%$$ (Equation 1)

where Δm is the difference of weight after and before adsorbing, ρ is the density of *n*-butanol, and V_0 is the volume of the separator.

Electrochemical measurements

CR2025-type coin cells were assembled in an open-air environment using Zn foil (thickness: 80 μm and diameter: 14 mm) as anode, the prepared electrodes as cathode, and 80 μL of 1 M ZnSO$_4$ as the electrolyte. The cyclic performances of all cells were collected by the Neware battery test system (CT-4008-5V20mA-164, Shenzhen, China). The other electrochemical performances were collected by the electrochemical workstation (chi760e, Shanghai, China). The electrochemical potential window were recorded using the linear sweep voltammetry (LSV) method with a scan rate of 1 mV s^{-1}. Tafel plots were measured by scanning between −0.3 and 0.3 V at 1 mV s^{-1}. The chronoamperometry (CA) curves were tested at an overpotential of −150 mV. The cyclic voltammetry (CV) curves were tested from 0.4 to 1.35 V at 0.1 mV s^{-1}. The ionic conductivities of the electrolytes were measured by electrochemical impedance spectroscopy (EIS) tests with a frequency range from 0.01 Hz to 10^5 Hz, and calculated through the equation:

$$\sigma\ =\ \frac{L}{RA}$$ (Equation 2)

where L is the thickness, A is electrode contact area, and R is bulk resistance.

The transference number of Zn^{2+} was obtained according to the typical Evans method, which should be described as the following formula:

$$t_{Zn^{2+}}\ =\ \frac{I_S(\Delta V\ -\ I_0 R_0)}{I_0(\Delta V\ -\ I_S R_S)}$$ (Equation 3)

where I_0/I_s and R_0/R_s represent the initial/final current density and charge transfer resistance before and after the chronoamperometry test, ΔV (20 mV) is the constant polarization potential for the chronoamperometry test.

Calculation method

The geometry optimizations and binding energy calculations based on density functional theory (DFT) were carried out using generalized gradient approximation (GGA) and Perdew-Burke-Ernzerhof (PBE) exchange-correlation functional[36] in Dmol3 module[37,38] of Materials Studio of Accelrys Inc. Grimme's DFD-D3 method[39] was used to represent the dispersion interactions. The convergence tolerance was set to 10^{-5} eV per atom for energy, 3.0×10^{-2} eV Å^{-1} for maximum force, and 10^{-3} Å for maximum displacement. The binding energy (E_b) between Zn^{2+} and different construction was calculated according to the following equations:

$$E_b\ =\ E_{total}\ -\ E_a\ -\ E_b$$ (Equation 4)

where E_{total} represents the total energy of the specific construction combined with Zn^{2+}, E_a and E_b represent the energy of Zn^{2+} and the energy of combined construction (water or molecular of separator components).

Simulation method

The simulation of the electric field distribution at the surface of the Zn anode was established in COMSOL software via a simplified 2D model. The Butler-Volmer equation without concentration polarization was used to analyze the relationship between interfacial current and potential:

$$j\ =\ j_0\left(\exp\left(\frac{\beta F \eta}{RT}\right)\ -\ \exp\left(\frac{(1-\beta)F\eta}{RT}\right)\right)$$ (Equation 5)

where j is the local current density, j_0 is the exchange current density, η is the overpotential, β is the anodic transfer coefficient, and $1-\beta$ is the cathodic transfer coefficient.

Ohm formula is used to analyze the relationship between current and potential in electrolyte region:

$$i\ =\ -\ \sigma \nabla \varphi$$ (Equation 6)

where i is the current of the electrolyte, σ is the ionic conductivity of the electrolyte, and φ is the potential of the electrolyte.

The size of the defined Zn anode model and electrolyte model is 50 μm × 20 μm and 50 μm × 30 μm, respectively. According to SEM images, the Zn dendrites model is constructed into round triangles with the diameter of 5 μm and 1 μm. According to experimental data, the ionic conductivities of the ZnSO$_4$ electrolyte were set to 0.398 S m^{-1} and 0.134 S m^{-1}. The j_0 of ZnSO$_4$ electrolyte was set to 0.805 mA cm^{-2} and 0.060 mA cm^{-2}. The electrical conductivity of Zn was set to 1.66 × 10^7 S m^{-1}.